Using in-situ solar-wind observations to generate inner-boundary conditions to outer-heliosphere simulations, 1: dynamic time warping applied to synthetic observations

Owens, M. ORCID: https://orcid.org/0000-0003-2061-2453 and Nichols, J. (2021) Using in-situ solar-wind observations to generate inner-boundary conditions to outer-heliosphere simulations, 1: dynamic time warping applied to synthetic observations. Monthly Notices of the Royal Astronomical Society, 508 (2). pp. 2575-2582. ISSN 0035-8711 doi: 10.1093/mnras/stab2512 Available at https://centaur.reading.ac.uk/100023/

To link to this article DOI: http://dx.doi.org/10.1093/mnras/stab2512

Publisher: Oxford Journals

Monthly Notices
of the
ROYAL ASTRONOMICAL SOCIETY

MNRAS **508,** 2575–2582 (2021)
Advance Access publication 2021 September 16

https://doi.org/10.1093/mnras/stab2512

Using *in situ* solar-wind observations to generate inner-boundary conditions to outer-heliosphere simulations – I. Dynamic time warping applied to synthetic observations

Mathew J. Owens 1★ and Jonathan D. Nichols[2]

[1]*Department of Meteorology, University of Reading, Earley Gate, Reading RG6 6BB, UK*
[2]*Physics and Astronomy Department, University of Leicester, University Road, Leicester LE1 7RH, UK*

Accepted 2021 September 2. Received 2021 September 2; in original form 2021 June 25

ABSTRACT

The structure and dynamics of the magnetospheres of the outer planets, particularly Saturn and Jupiter, have been explored through both remote and *in situ* observations. Interpreting these observations often necessitates simultaneous knowledge of the solar-wind conditions impinging on the magnetosphere. Without an available upstream monitor, solar-wind context is typically provided using models initiated with either the output of magnetogram-constrained coronal models or, more commonly, *in situ* observations from 1 au. While 1-au observations provide a direct measure of solar-wind conditions, they are single-point observations and thus require interpolation to provide inputs to outer-heliosphere solar-wind models. In this study, we test the different interpolation methods using synthetic 1-au observations of time-evolving solar-wind structure. The simplest method is 'corotation', which assumes solar-wind structure is a steady state and rotates with the Sun. This method of reconstruction produces discontinuities in the solar-wind inputs as new observations become available. This can be reduced by corotating both backwards and forwards in time, but this still introduces large errors in the magnitude and timing of solar-wind streams. We show how the dynamic time warping (DTW) algorithm can provide around an order-of-magnitude improvement in solar-wind inputs to the outer-heliosphere model from *in situ* observations near 1 au. This is intended to build the foundation for further work demonstrating and validating methods to improve inner-boundary conditions of outer-heliosphere solar-wind models, including dealing with solar-wind transients and quantifying the improvements at Saturn and Jupiter.

Key words: Sun: heliosphere – solar wind – planet–star interactions.

1 INTRODUCTION

The magnetospheres of Saturn (Dougherty, Esposito & Krimigis 2009) and Jupiter (Bagenal et al. 2004) have been explored both through remote observations and with *in situ* spacecraft observations (e.g. Crary et al. 2005; Clarke et al. 2009; Hess, Echer & Zarka 2012; Connerney et al. 2017). Though the dynamics of the outer planets' magnetospheres are rotationally dominated, they are strongly modulated by the solar wind, so, like at the Earth, understanding the dynamics of these magnetospheric systems requires simultaneous knowledge of the local solar-wind conditions (Brice & Ioannidis 1970; Kennel & Coroniti 1975; Nichols, Cowley & McComas 2006; Badman & Cowley 2007; Delamere & Bagenal 2010; Masters 2015; Nichols et al. 2017). In the absence of such available observations, this must instead be provided by solar-wind models.

Solar-wind conditions in near-Earth space are routinely forecast based on photospheric observations, through coupled coronal and heliospheric models (e.g. Riley, Linker & Mikic 2001; Odstrcil 2003; Toth et al. 2005; Merkin et al. 2016; Pomoell & Poedts 2018). However, for outer-planet research, genuine forecasting is rarely required, and the accuracy of the solar-wind structure reconstructed by magnetogram-based methods may not be sufficient (e.g. Owens et al. 2008). Thus, the preferred method is to propagate *in situ* observations from 1 au to the required planetary target. Over short radial distances, this can be done ballistically (Vennerstrom et al. 2003). However, the solar-wind undergoes a great deal of dynamic evolution between 1 and 5–10 au (e.g. Hanlon et al. 2004), which we here refer to as the outer heliosphere. Thus, the propagation of available observations is typically done using numerical fluid models, with magnetohydrodynamic (MHD) models used in both one-dimensional (1D) (Tao et al. 2005; Zieger & Hansen 2008) and 2D [e.g. the MSWIM2D models, based on the Toth et al.

★ E-mail: m.j.owens@reading.ac.uk

(2005) framework; see also Keebler (2021)]. This general approach supports a huge volume of planetary science (e.g. Zarka et al. 2007; Clarke et al. 2009; Nichols et al. 2009; Kimura et al. 2013; Provan et al. 2015; Kita et al. 2016).

As 1-au observations are rarely available in perfect radial alignment with the target planet, observations also have to be extrapolated in longitude. This is true for 1D models (Tao et al. 2005; Zieger & Hansen 2008), where either the model inputs or outputs can be extrapolated between the observation longitude and the target longitude, or for 2D models (Keebler 2021), where all longitudes must be reconstructed from the available single-point observations to provide a full set of inner-boundary conditions at 1 au. In both cases, 'corotation' is used, wherein the conditions at a given Carrington longitude (i.e. in a frame rotating with the Sun) are assumed to be equal to previous or subsequent observations at the same Carrington longitude. Thus, the assumption is made of no time evolution.

The simplest form of corotation uses the previous observation at a required longitude, i.e. it looks only back in time, which enables it to also be used for forecasting (e.g. Kohutova et al. 2016; Thomas et al. 2018; Turner et al. 2021). When the solar-wind structure (in the rotating frame of the Sun) is evolving with time, this produces sharp discontinuities in the reconstructed solar wind at longitudes where new observations are introduced. To mitigate this, corotation can be 'smoothed' in time (and hence Carrington longitude) by interpolating between the previous and subsequent observations at a given longitude. This approach is used by the most recent implementation of the 2D MSWIM2D model (Keebler 2021).

In this study, we produce synthetic *in situ* observations from a model of time-evolving solar wind and test how well the corotation schemes can reconstruct the true state. It is shown that the time-smoothing form of corotation produces an improvement over simple corotation, greatly reducing the artificial discontinuities, but that there are still significant errors in reconstructing a time-evolving solar-wind structure. Ideally, the strengths of the magnetogram-constrained solar-wind models would be combined with the information from *in situ* observations using data assimilation (Lang & Owens 2019; Lang et al. 2021). However, this is currently possible only with reduced-physics models, and is computationally intensive for the long runs required for outer-heliosphere simulations. While these techniques will become more accessible in the future, in this study, we explore an alternative method for best exploiting *in situ* observations as inner-boundary conditions to outer-heliosphere solar-wind simulations.

To explicitly allow for time evolution, we develop a reconstruction scheme based on dynamic time warping (DTW). This method is explained in Section 2 and tested in Section 3. This study is intended to be the first in a series examining how best to use 1-au observations to provide inner-boundary conditions to solar-wind models. Future papers will use the inner-boundary conditions generated in this study to drive solar-wind simulations and quantify the effect on the solar-wind conditions reconstructed at the orbits of Saturn and Jupiter, outline and test a scheme for dealing with transient structures from interplanetary coronal mass ejections (ICMEs) in the *in situ* observations, and apply the methods to real observations from near-Earth and*STEREO* spacecraft.

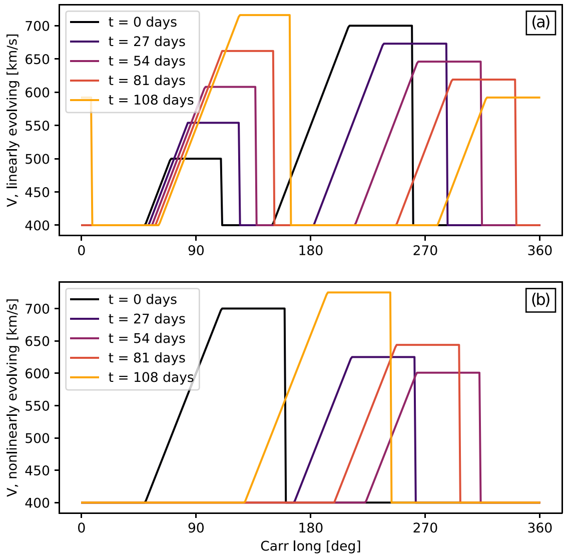

Figure 1. Two models of solar-wind speed evolution. Snapshots of solar-wind speed as a function of Carrington longitude are shown five times, approximately one Carrington rotation (CR) apart. Panel (a): Two fast solar-wind streams evolve linearly in magnitude, width, and position as a function of time. Panel (b): A single solar-wind stream evolves non-linearly in magnitude, width, and position as a function of time.

2 METHODS

2.1 Synthetic solar-wind observations

In order to test solar-wind reconstruction methods, we produce synthetic *in situ* observations from time-evolving models of solar-wind speed, V. This enables us to compare with the 'true' state from which synthetic observations are constructed, which is not possible with real observations.

Fig. 1 shows two models of V at the heliographic equator at 1 au, in the Carrington frame rotating with the Sun. Fig. 1(a) shows the linear model in which two fast streams both move in longitude and change in magnitude linearly with time. The properties of the fast streams are chosen arbitrarily and can be varied in the analysis code available through the GitHub link in the acknowledgements. In the example used here, we choose values typical of the solar wind observed at 1 au (e.g. Owens 2019). Slow wind has a speed of 400 km s^{-1}. The first fast stream has an initial amplitude of 700 km s^{-1} and begins at a maximum longitude of 260° with a width of 50°. The fast stream amplitude decays at a rate of 1 km s^{-1} per day and it moves to greater Carrington longitude at a rate of 1° per day. The second fast stream has an amplitude of 500 km s^{-1}, increasing at 2 km s^{-1} per day, a width of 40°, and an initial longitude of 110°, increasing at 0°.5 per day. The maximum and minimum allowed speeds are capped at 800 and 400 km s^{-1}, respectively. Both fast streams have a declining V back to the slow wind speed at a gradient of 5 km s^{-1} per degree of longitude. As a (quasi-) stationary spacecraft at 1 au moves to smaller Carrington longitude with time, these profiles produce V time series of fast streams with a discontinuous rise in solar-wind speed, followed by a constant peak V, before linearly declining back to slow wind.

We also consider a non-linear model in which both the longitude and magnitude of the fast stream vary sinusoidally, as shown in Fig. 1(b). In the example shown, there is a slow wind of speed 400 km s^{-1}, with a single fast stream. The fast stream has a width of

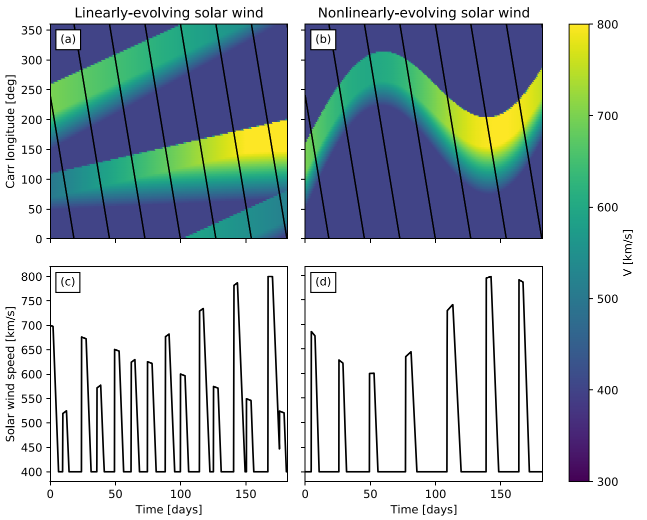

Figure 2. Two models of solar-wind speed evolution. Left-hand panels: linearly evolving *V* with time. Right-hand panels: non-linearly evolving *V* with time. Top panels: colour maps of solar-wind speed as a function of Carrington longitude and time. The Earth's position is shown by the black lines. Bottom panels: the resulting *V* time series in near-Earth space.

50° and initially has a maximum longitude of 160°. The longitude varies sinusoidally with an amplitude of 100° and a period of 200 d, as well as drifting linearlyto greater longitude at a rate of 1° per day. The amplitude of the fast stream is initially 600 km s^{-1}, varying sinusoidally with an amplitude of 100 km s^{-1} and a period of 200 d.

The *V* obtained by these two models is shown as a function of Carrington longitude and time in Figs 2(a) and (b). In this format, a non-evolving solar wind would show horizontal bands of constant *V*. The black lines show the Earth's position, at which the synthetic *V* time series is extracted and shown in Figs 2(c) and (d). We next test the ability of various techniques to reconstruct *V* at all Carrington longitudes from this synthetic near-Earth *V* time series.

2.2 Corotation reconstruction methods

Cororation is the most commonly used technique to reconstruct solar-wind conditions at longitudes distant from that where observations are available. Corotation assumes that the solar-wind structure in the rotating frame of the Sun does not change with time. It is illustrated schematically in Fig. 3(a). The thick diagonal lines track the position of Earth over two subsequent CRs, CR *N* and $N + 1$. The transition from red to blue shows an observed transition from slow to fast wind in near-Earth space. The slow–fast wind interface moves to a larger Carrington longitude (ϕ) with time, and thus the reconstruction point (t_0, ϕ_0) where the solar wind is to be reconstructed is in fast wind. Standard corotation looks back into the previous CR to find the previous *V* observation at ϕ_0, which occurred at a time t_-. Therefore, the reconstructed *V* at (t_0, ϕ_0) by corotation backwards in time, V_{CB}, is given by

$$V_{\mathrm{CB}}(t_0, \phi_0) = V(t_-, \phi_0). \quad (1)$$

In the example shown in Fig. 3(a), the time evolution means that corotation (backwards in time) incorrectly estimates $V_{\mathrm{CB}}(t_0, \phi_0)$ to be slow wind.

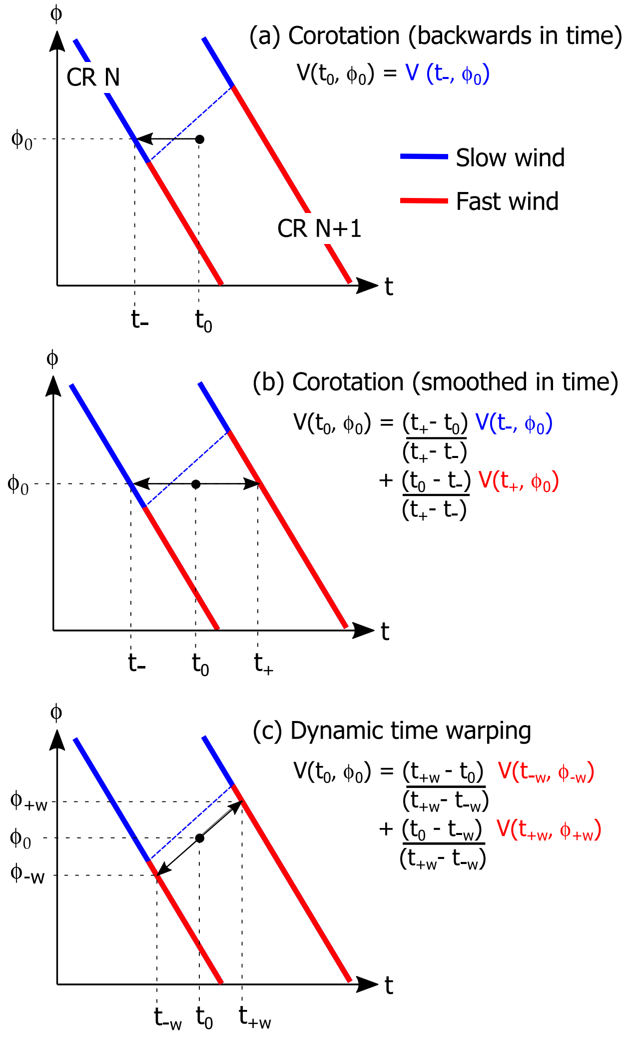

Figure 3. Schematics of the three reconstruction methods assessed in this study. Two CRs of *in situ* observations are shown as a function of Carrington longitude, ϕ, and time, *t*, with the slow/fast wind in blue/red. Slow–fast-wind interface (blue dashed line) moves to greater ϕ between CR *N* to CR $N + 1$. The reconstruction point, (t_0, ϕ_0), shown as a black dot, is in fast wind. Panel (a): In the standard corotation method, $V(t_0, \phi_0)$ is equal to the value at the same Carrington longitude at the time of the previous observation. In this example, it gives slow wind. Panel (b): Corotation smoothed in time uses a weighted average of the prior and subsequent values of *V* at ϕ_0, which results in intermediate-speed wind. Panel (c): DTW aligns features in the CR *N* and CR $N + 1$ time series and takes a weighted average along the determined warp path. This results in fast wind at *V*, as required.

For reconstruction (i.e. in non-forecast situations), corotation can be applied both forwards and backwards in time to find the prior and subsequent *V* at the same Carrington longitude. A weighted average (based on timing proximity) of the two *V* values is taken. We refer to this as 'corotation time smoothing'. It is schematically shown in Fig. 3(b). The estimated speed by this method, V_{CT}, is given by

$$V_{\mathrm{CT}}(t_0, \phi_0) = \frac{t_+ - t_0}{t_+ - t_-} V(t_-, \phi_0) + \frac{t_0 - t_-}{t_+ - t_-} V(t_+, \phi_0), \quad (2)$$

where t_+ is the time of the *V* observation at Carrington longitude ϕ_0 during the subsequent CR.

In the example shown in Fig. 3(b), the corotation time smoothing would produce intermediate-speed solar wind at the reconstruction point.

2.3 Reconstruction by the DTW

As will be shown in Section 3, corotation time smoothing provides improved reconstruction over simple back-in-time corotation, but it still does not explicitly account for the time evolution of solar-wind structures. Here, we match solar-wind structures in consecutive time series bounding the required reconstruction time/position to explicitly allow for time evolution. The principle is shown schematically in Fig. 3(c). If features, such as the slow/fast solar-wind transition, can be connected between subsequent time series, then the time smoothing can be performed along 'connection lines' rather than along constant Carrington longitude lines. In the example shown, this would correctly identify fast wind at the reconstruction point.

In order to systematically determine the connections between solar-wind streams in two time series, we use an algorithm called 'dynamic time warping' (Sakoe & Chiba 1978; Keogh & Ratanamahatana 2005). DTW is used to measure similarity between temporal profiles, and is commonly used in automatic speech recognition to look for similar waveforms when people have different speech cadences. In geophysics, it can also be used as a metric of the agreement of two time series (Laperre, Amaya & Lapenta 2020), without overpenalizing for small timing errors (Owens 2018). It has also been proposed as a way to project solar-wind stream fronts from observing spacecraft at the L1 point to the nose of the Earth's magnetosphere (Prchlik & Stevens 2018). Here, DTW will be used to assess the connection lines (or 'warp paths') that connect similar features in two time series. For this purpose, we use the Meert, Hendrickx & Craenendonck (2020) implementation in PYTHON.

In brief, DTW can be summarized as follows: For two data sequences, A (a_1, a_2, a_3, ..., a_M) and B (b_1, b_2, b_3, ..., b_N), we seek to match every index in A with one or more indices in B in a way that minimizes the difference between the two sequences. This matching is subject to a number of rules (here written only for sequence A, though they also apply to B):

(i) Every index in A must be matched with one or more indices in B.

(ii) a_1 must map to b_1, though it may also map to larger indices in B.

(iii) a_M must map to b_N, though it may also map to smaller indices in B.

(iv) Mapping must be monotonically increasing; that is, if a_i maps to b_j, then a_{i+1} must map to either b_j and/or b_{j+1} (and possibly also higher B indices).

A cost function, based on the difference between the mapped indices, is then minimized to give the optimal match. Additional constraints can also be used. It is common to impose a locality constraint, such that mappings between a_i and b_j must meet the criterion $|i - j| < w$, where w is the maximum window length over which mapping is permitted.

An example of DTW applied to two V time series is shown in Fig. 4. Panels (a) and (b) show V at Earth produced by the linearly evolving solar-wind model for two consecutive CRs, N and $N+1$, respectively. Fig. 4(c) shows the cumulative Euclidean distance between the V values when different sections of the time series are aligned. This alignment is not a fixed time offset, but a variable 'warping' of the time series. If there was no time evolution, the optimum path (shown in black) would lie along the $y = x$ line (shown in white). During long intervals of slow wind, such as days 20–25, there are no features for the algorithm to match and a low cumulative distance can be achieved for a large range of different warpings. At the slow–fast-wind interface, however, such as around days 2 and 14, there is a very clear optimum warping. In both cases, the structure in CR N is encountered earlier than in CR $N+1$. Thus, the sharp gradients in V act as 'anchor points' for the DTW scheme. As discussed further in Section 4, at times when there is little structure in V, it may be necessary to use additional solar-wind parameters to provide the required anchor points and produce accurate warp paths between the two time series.

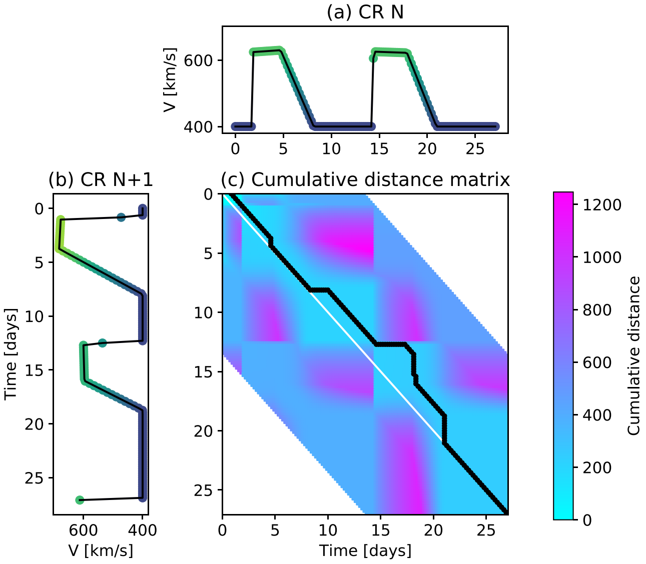

Figure 4. An example of DTW applied to two near-Earth V time series produced by the linearly evolving model. Panel (a) shows the time series of V for CR N, while panel (b) shows the time series of V for CR $N+1$. Fast/slow wind is further highlighted by yellow/blue. Panel (c) shows a colour map of the total distance between time points for all possible connections. The black line traces the optimal path (i.e. minimum cumulative distance). For this example, most warp paths connect to earlier times in CR $N+1$, suggesting solar-wind features are moving earlier in the CR. The optimal path is best constrained at the leading edge of fast streams.

The same example time series are shown in Fig. 5 as a function of Carrington longitude and time, with V as the colour scale. The black lines show identified optimal warp paths between the V time series. As the fast solar-wind streams are moving to increasing Carrington longitude between the two CRs, most of these connection lines have a positive gradient. At the point of interest, shown as a red dot, the closest connector is shaded red. It connects fast solar wind at both ends and thus (correctly) predicts fast wind at the reconstruction point. However, the exact magnitudes of V at the start and end of the best warp path are different, so we take a weighted average:

$$V_{\mathrm{DTW}}(t_0, \phi_0) = \frac{t_{+\mathrm{W}} - t_0}{t_{+\mathrm{W}} - t_{-\mathrm{W}}} V(t_{-\mathrm{W}}, \phi_{-\mathrm{W}}) + \frac{t_0 - t_{-\mathrm{W}}}{t_{+\mathrm{W}} - t_{-\mathrm{W}}} V(t_{+\mathrm{W}}, \phi_{+\mathrm{W}}), \tag{3}$$

where $t_{-\mathrm{W}}$ and $t_{+\mathrm{W}}$ are the times of the start and end of the optimal warp paths, respectively, and $\phi_{-\mathrm{W}}$ and $\phi_{+\mathrm{W}}$ are the associated Carrington longitudes.

For each time and longitude at which V is to be reconstructed, we produce two 27-d time series at 1-h resolution from the synthetic near-Earth V, centred on t_+ and t_-. We apply DTW to these two time series, allowing 5 d at the start and end of the time series to be ignored if it produces a lower average distance, so as to minimize edge effects. We also set a maximum warp window of 5 d, to avoid

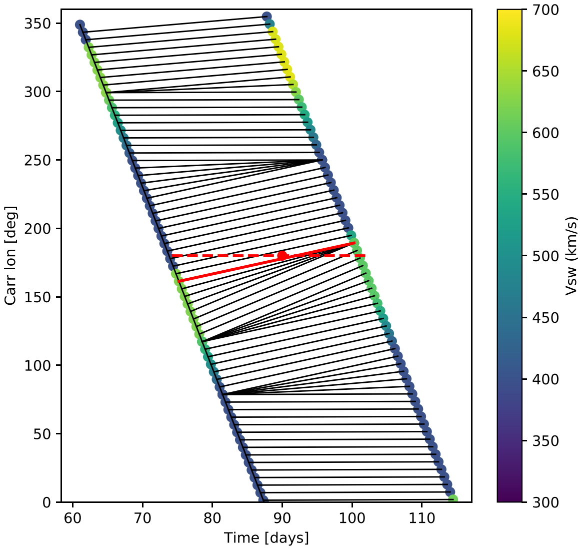

Figure 5. An example of DTW reconstruction applied to subsequent CRs of near-Earth *V* observations obtained from the linearly evolving *V* model. The red dot shows the position/time where *V* is to be reconstructed. Corotation uses previous/subsequent observed values in near-Earth space at the same Carrington longitude, shown by the dashed red line. The black lines show the DTW warp paths that best connect the *V* time series at subsequent CRs. The DTW estimate of solar wind uses observed values along the closest warp path, shown by the solid red line.

connecting different solar-wind streams. This means that DTW will not be able to recognize very rapid solar-wind evolution. The results presented here are insensitive to the choice of these parameters. Optimal smoothing of the input time series and choice of the edge- and warp-windows for use with real *in situ* data will be invested in a future paper in this series.

3 RESULTS

Figs 6 and 7 show solar-wind speed as a function of Carrington longitude and time obtained by applying the three reconstruction techniques to the synthetic near-Earth observations. Reconstructions are made at daily cadence and for 128-longitude bins, though results are unchanged at hourly resolution and 720-longitude bins.

Figs 6(b) and 7(b) clearly show that in the presence of time-evolving solar-wind structures, corotation (backwards in time) produces discontinuities in the reconstructed solar wind as new observations are introduced. When performing 2D solar-wind modelling, this produces unphysical solar-wind solutions, as will be demonstrated and quantified in a later paper in this series. By comparing the two fast streams in the linear case (Fig. 6b), it is also apparent that the issues with corotation are greater for features that are evolving faster in time.

Figs 6 and 7 show that time-smoothing corotation does indeed reduce discontinuities in *V* relative to corotation back in time when new observations are introduced. However, there are still visible artefacts, particularly for the fast-evolving solar-wind streams.

The result of the DTW reconstruction method applied to the linearly evolving solar wind is shown in Fig. 6(d). The agreement with the true state (Fig. 6a) appears, by eye, to be very good. In particular, there are no apparent artefacts at the observation locations, which are obvious for both the simple corotation back in time and the time-smoothing corotation methods.

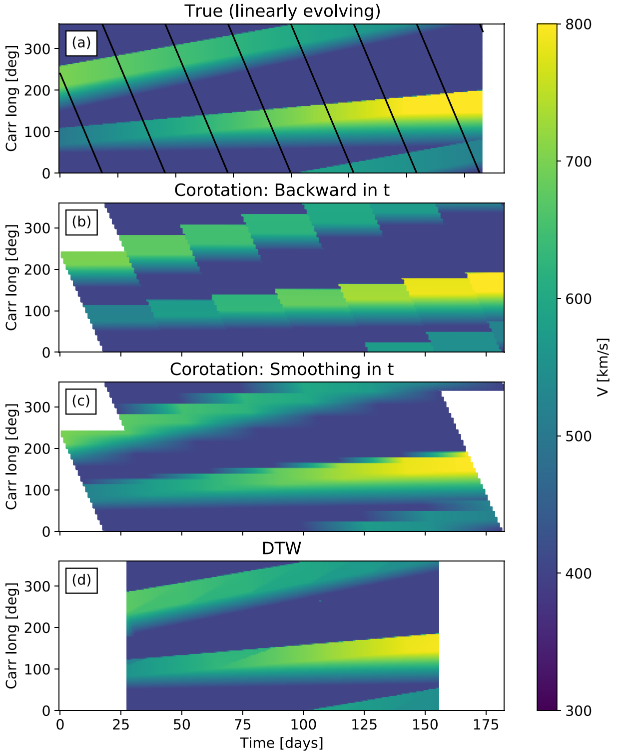

Figure 6. Solar-wind speed as a function of longitude and time. Panel (a): the model of linearly evolving solar-wind structure from which synthetic *V* time series are produced in the Earth's orbit (black lines). The bottom three panels show *V* reconstructed from synthetic near-Earth observations by three methods. Panel (b): corotation backwards in time, panel (c): corotation smoothed backwards and forwards in time, and panel (d): DTW.

For the non-linear solar-wind evolution, shown in Fig. 9, DTW again provides a better visual match than either of the corotation methods. However, unlike the linear case, the location of observations can be seen in the DTW reconstruction as a change in gradient in the longitude of the fast stream with time.

In order to visualize these differences more clearly, we also compute d*V*, the difference between the true state and the reconstruction. The linearly evolving solar wind is shown in Fig. 8. The large positive and negative d*V* values for the two corotation methods (Figs 8a and b, respectively) are almost completely removed by DTW (Fig. 8c). The average values over the whole domain, between times of 27 and 157 d, are summarized in Table 1. The time-smoothing corotation produces average errors about a factor of 2.5 lower than backward-in-time corotation. DTW provides nearly an order-of-magnitude further reduction in average errors from time-smoothing corotation.

Fig. 9 shows d*V* for the non-linearly evolving solar wind. For DTW, the errors are largely confined close to the high-speed stream front, whereas they are spread over a greater longitude range for the corotation methods. Table 1 shows that the time-smoothing corotation produces average errors about a factor of 2 lower than backward-in-time corotation, with DTW providing a further factor of 2 reduction from time-smoothing corotation.

It is instructive to look in more detail at the reconstructed *V* time series at locations distant from observations. Fig. 10 shows the time series reconstructed 180° ahead of the Earth in its orbit (i.e. at the longitude farthest from available observations). For both the

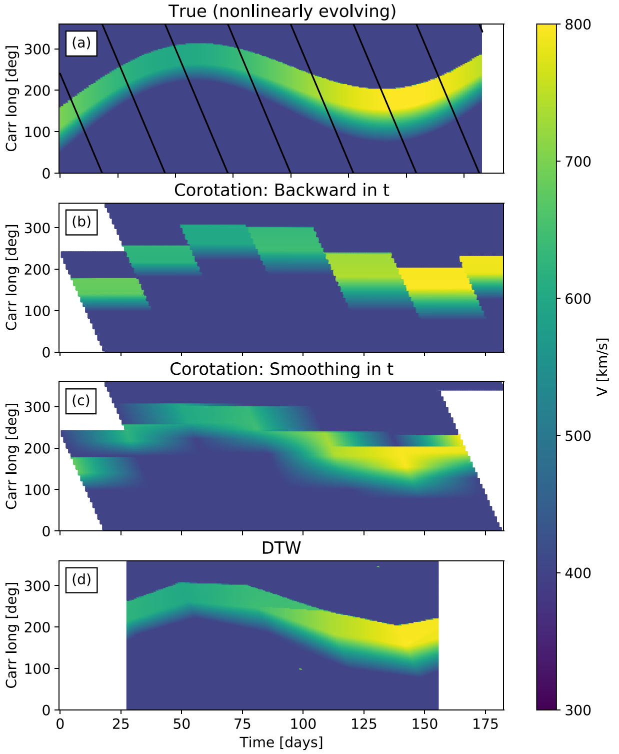

Figure 7. Solar-wind speed as a function of longitude and time. Panel (a): the model of non-linearly evolving solar-wind structure from which synthetic V time series are produced in the Earth's orbit (black lines). The bottom three panels show V reconstructed from synthetic near-Earth observations by three methods. Panel (b): corotation backwards in time, panel (c): corotation smoothed backwards and forwards in time, and panel (d): the DTW.

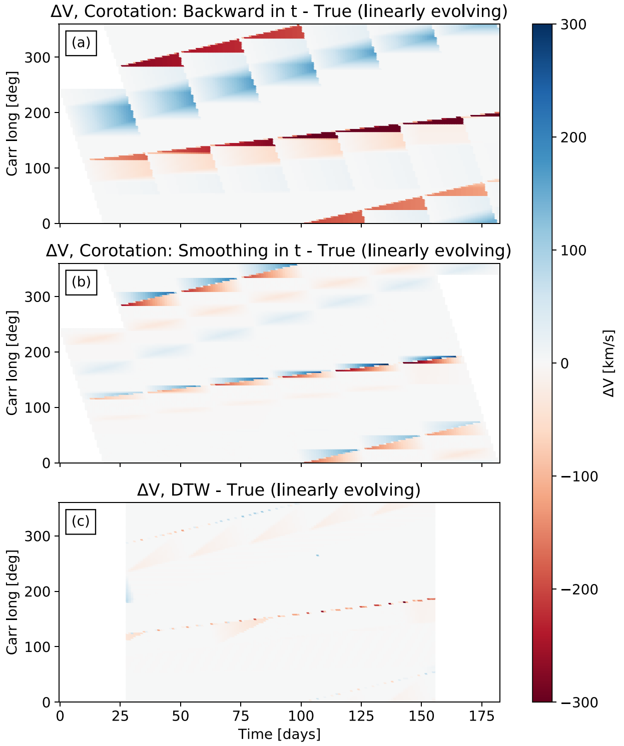

Figure 8. The V error between the reconstruction methods and the true state of the linearly evolving solar wind, as a function of Carrington longitude and time. Panel (a): corotation backwards in time. Panel (b): corotation smoothed backwards and forwards in time. Panel (c): DTW.

Table 1. The mean absolute error (MAE) in V between the true state and the reconstructed state from synthetic near-Earth time series. Values are computed between days 27 and 157, when all methods are valid.

	$\langle \lvert \Delta V \rvert \rangle$ (linear)	$\langle \lvert \Delta V \rvert \rangle$ (non-linear)
Corotation (backwards in t)	$28.5\,\mathrm{km\,s^{-1}}$	$35.0\,\mathrm{km\,s^{-1}}$
Corotation (smoothed in t)	$11.0\,\mathrm{km\,s^{-1}}$	$17.1\,\mathrm{km\,s^{-1}}$
DTW	$1.8\,\mathrm{km\,s^{-1}}$	$8.3\,\mathrm{km\,s^{-1}}$

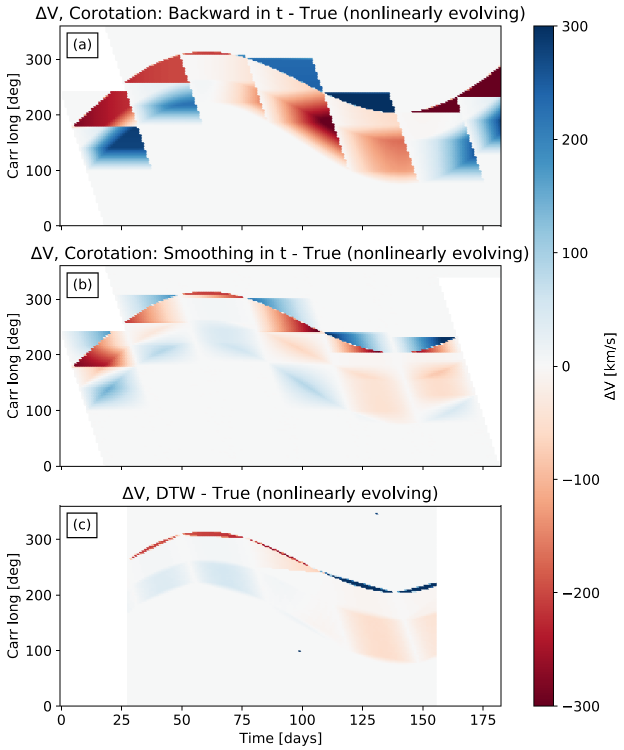

Figure 9. The V error between the reconstruction methods and the true state of the non-linearly evolving solar wind, as a function of Carrington longitude and time. Panel (a): corotation backwards in time. Panel (b): corotation smoothed backwards and forwards in time. Panel (c): DTW.

linear and non-linear cases, corotation back in time (green lines) reproduces the correct general form of the solar-wind structure, but with systematic timing and/or magnitude offsets in the high-speed streams.

The systematic timing errors are also generally removed by time smoothing the corotation reconstruction (blue lines). However, the time profile of the high-speed stream has been altered. For the non-linearly evolving solar wind shown in Fig. 10(b), the true state (black line) shows a single rise in V at day 92.5, whereas time smoothing produces both a jump to the left (at day 90) and a step to the right (at day 96). This results from different V values obtained from averaging the backwards and forwards in time corotations to give intermediate-speed wind, matching neither observation. This results in the two-step V time series profile for the high-speed streams. In a later paper, the effect of this on the reconstructed solar wind on the outer planets will be quantified.

The timing, magnitude, and waveform of the DTW reconstructed fast streams (red dashed lines) are in better agreement with the true state than the corotation methods. For the non-linearly evolving solar wind (Fig. 10b), it can be seen that the dV at the leading edge

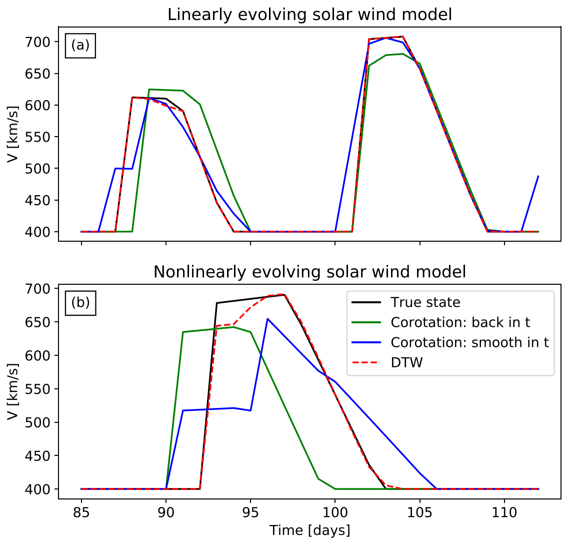

Figure 10. Example of *V* time series from a point 180° ahead of the Earth in its orbit (i.e. the farthest point from an available observation). Panel (a): linearly evolving solar-wind model. Panel (b) the non-linearly evolving solar-wind model. Black lines show the true state. Coloured lines show the reconstructed values using the near-Earth *V* time series using (green) corotation back in time, (blue) corotation smoothed backwards and forwards in time, and (red dashed line) DTW.

of the fast stream is actually a small magnitude error, rather than the timing errors present for the corotation methods.

Fig. 10 considers only a single location relative to the Earth. In order to look more generally at the performance of the reconstruction methods, we produce time series for the true state and reconstructions at a range of longitudes relative to the Earth, $\Delta\phi$. These are summarized in Fig. 11.

For each time series, we compute the MAE in *V*, shown in Figs 11(a) and (b) for the linearly and non-linearly evolving solar winds, respectively. For corotation back in time (green lines), the MAE increases almost linearly with $\Delta\phi$, and produces a large discontinuity at the $\Delta\phi = 0^\circ/360^\circ$ position. Corotation smoothed in time removes this discontinuity, with MAE = 0 at $\Delta\phi = 0^\circ$ and $\Delta\phi = 360^\circ$. MAE is maximized at $\Delta\phi = 180^\circ$. MAE for DTW (red lines) exhibits the same basic behaviour, but with reduced amplitude.

We also apply high-speed enhancement (HSE) analysis to each time series (Owens et al. 2005; MacNeice 2009; MacNeice et al. 2018). This event-based analysis identifies an HSE using a minimum speed gradient, then associates HSEs between the observed and reconstructed time series. This allows us to determine the timing and magnitude errors in individual high-speed streams. Figs 11(c) and (d) show that corotation back in time introduces timing errors, ΔT, which grow linearly with $\Delta\phi$. For the non-linearly evolving solar wind, corotation smoothed in time shows similar behaviour to MAE. For the linear case, however, ΔT peaks at low $\Delta\phi$ at a value larger than corotation back in time, then declines with $\Delta\phi$. This is due to the two-step *V* profile, with an HSE analysis jumping between defining the event start between the first and second increases in *V*. For DTW, ΔT is effectively zero for the linear case, but peaks at $\Delta\phi = 180^\circ$ in the non-linear case, though again at lower values than either of the corotation methods. The HSE magnitude errors, ΔV, are shown in Figs 11(e) and (f). Of note is the ΔV for corotation smoothed in time in the non-linearly evolving solar wind case (i.e. the blue line in Fig. 11f). There is a sharp peak in ΔV around $\Delta\phi = 180^\circ$. This is due to time smoothing introducing an artifical two-step waveform at solar wind speed gradients (as seen in Fig. 10b). The HSE is consequently identified as only the first step up in speed, producing a low maximum speed.

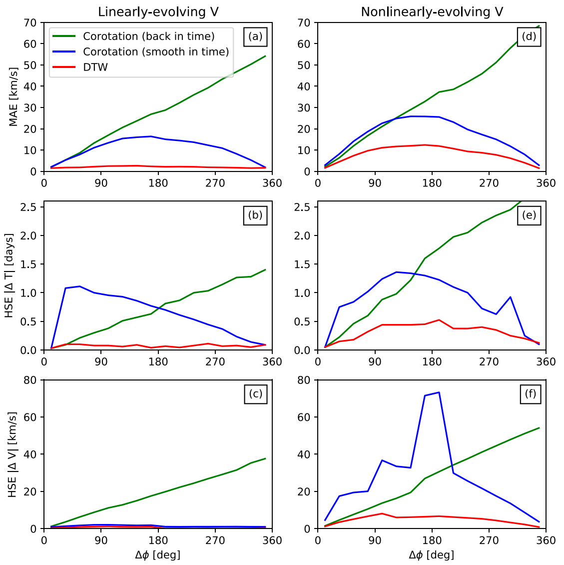

Figure 11. Metrics for the three reconstruction methods at different longitudes relative to Earth, $\Delta\phi$. Left- and right-hand panels show the linearly and non-linearly evolving solar winds, respectively. Panels (a) and (b): the mean-absolute error in *V*. Panels (c) and (d): timing error, ΔT, in the high-speed streams. Panels (e) and (f): magnitude error, ΔV, in the high-speed streams. Green lines show corotation back in time, blue lines show corotation smoothed in time, and red lines show DTW.

4 CONCLUSIONS

Observations of planetary magnetospheres benefit from the local solar-wind context. For the outer planets, this is typically provided using solar-wind models initiated from *in situ* observations around 1 au. This is Paper I in a series, which investigates and validates methods for reconstructing the solar-wind speed, *V*, at all longitudes from single-point *in situ* observations. The standard method is corotation in which *V* at a given Carrington longitude is equal to the last available observation at that longitude. Thus, corotation-based reconstruction assumes no time variation in solar-wind structure. In order to quantify the effect of this, and explore a technique that relaxes the time-stationary assumption, we constructed two models of the solar-wind evolution and produced synthetic *in situ* observations from which the global structure is to be reconstructed: one in which the solar wind structure evolves linearly with time and the other in which the solar-wind structure evolves non-linearly.

Using these models, time smoothing – in which the reconstructed speed at a given point is a linear combination of the corotated speed both forwards and backwards in time – is shown to greatly improve *V* reconstruction over the standard corotation back in time. In particular, the discontinuity in reconstructed *V* produced by the introduction of new observations is greatly reduced by the use of time smoothing. However, there are still issues, particularly in reconstructing the non-linearly evolving solar wind. In general, corotation with time smoothing removes systematic offsets in the timing of fast streams, but changes the waveform of reconstructed fast streams, spreading them over a longer time interval and reducing the peak amplitude.

To address these issues, we adapt a data analysis technique employed in automatic speech recognition to account for different speech cadences. DTW computes the agreement between temporal profiles when connecting different points within the profile. By finding the 'warp path' that maximizes the agreement, we are able to interpolate between the same solar-wind structures, rather than solar wind at the same Carrington longitudes. Applying the DTW method to the linearly evolving solar wind produces an almost perfect reconstruction, with an order-of-magnitude reduction in V errors even compared to corotation time smoothing. For the non-linear case, the improvements were not as large, but still significant over the corotation methods. The implications for using these boundary conditions for solar-wind prediction on the outer planets will be investigated using the HUXt solar-wind model (Owens et al. 2020) in future work, though the results are expected to be generally applicable to any model using the same input boundary conditions.

We note that real *in situ* observations can contain transient structures in the form of ICMEs. Assuming ICMEs repeat in subsequent CRs, or are seen by spacecraft that are well separated in longitude, will create major errors in corotation-based schemes and will produce incorrect warping paths in the DTW approach. Methods to deal with transient features will be investigated in a subsequent paper in the series.

For simplicity, this study has only looked at solar-wind speed and synthetic observations from a single spacecraft. The same methodology can be applied to multiple spacecraft observations near 1 au, as will later be demonstrated using near-Earth and *STEREO* observations.

The warping paths determined from V observations can be applied to other solar-wind parameters, allowing a full set of input conditions for MHD models (e.g. Tao et al. 2005; Zieger & Hansen 2008). (Note that it would not be desirable to determine and apply different warp paths for different solar-wind parameters, as this would result in unphysical solutions, For example, potentially moving a period of the southward heliospheric magnetic field from a fast to slow solar-wind region.) We also note that it is possible to determine a single set of warp paths from the matching of multiple time series. Thus, it is possible to find a single set of warp paths that provide the best match to multiple solar-wind parameters, such as speed, magnetic field polarity, and density. This will be beneficial if the DTW method is underconstrained by insufficient common 'anchor points' within a single parameter time series. For the synthetic time series considered in this study, this was not an issue. Unambiguous testing of the method with real solar-wind observations is difficult as the true state is not known. However, in the final paper in the series, we will determine the robustness of the warp paths as new information is provided. For real solar-wind observations, determining the most accurate warping paths may require pre-processing of the data, such as smoothing high-frequency 'noise'. This will also be investigated.

ACKNOWLEDGEMENTS

Work was part-funded by the Science and Technology Facilities Council (STFC) grant numbers ST/R000921/1 and ST/V000497/1 and part-funded by the Natural Environment Research Council (NERC) grant numbers NE/S010033/1 and NE/P016928/1.

DATA AVAILABILITY

No data were used in this study. All model and analysis code is available in the PYTHON language from www.github.com/University-of-Reading-Space-Science/SolarWindInputs_DTW.

REFERENCES

Badman S. V., Cowley S. W. H., 2007, Ann. Geophys., 25, 941

Bagenal F., Dowling T. E., McKinnon W. B., McKinnon W., 2004, Jupiter: The Planet, Satellites and Magnetosphere. Cambridge Univ. Press, Cambridge

Brice N. M., Ioannidis G. A., 1970, Icarus, 13, 173

Clarke J. T. et al., 2009, J. Geophys. Res., Space Phys., 114, A05210

Connerney J. E. P. et al., 2017, Science, 356, 826

Crary F. J. et al., 2005, Nature, 433, 720

Delamere P. A., Bagenal F., 2010, J. Geophys., Space Phys., 115, A10201

Dougherty M. K., Esposito L. W., Krimigis S. M., 2009, Saturn from Cassini-Huygens, 1st edn. Springer, Dordrecht

Hanlon P. G., Dougherty M. K., Forsyth R. J., Owens M. J., Hansen K. C., Toth G., Crary F. J., Young D. T., 2004, J. Geophys. Res., 109, A09S03

Hess S. L. G., Echer E., Zarka P., 2012, Planet. Space Sci., 70, 114

Keebler T., 2021, MSWIM2D: Outer Heliosphere Solar-wind Dataset. Whole Heliosphere & Planetary Interactions, UCAR, Boulder, USA

Kennel C. F., Coroniti F. V., 1975, in Formisano V., ed., The Magnetospheres of the Earth and Jupiter. Astrophysics and Space Science Library. Springer, Dordrecht, p. 451

Keogh E., Ratanamahatana C. A., 2005, Knowl. Inf. Syst., 7, 358

Kimura T. et al., 2013, J. Geophys. Res., Space Phys., 118, 7019

Kita H. et al., 2016, Geophys. Res. Lett., 43, 6790

Kohutova P., Bocquet F.-X., Henley E. M., Owens M. J., 2016, Space Weather, 14, 802

Lang M., Owens M. J., 2019, Space Weather, 17, 59

Lang M., Witherington J., Turner H., Owens M., Riley P., 2021, Space Weather,19, 29

Laperre B., Amaya J., Lapenta G., 2020, Frontiers Astron. Space Sci., 7, 39

MacNeice P., 2009, Space Weather, 7, S06004

MacNeice P. et al., 2018, Space Weather, 16, 1644

Masters A., 2015, Geophys. Res. Lett., 42, 2577

Meert W., Hendrickx K., Craenendonck T. V., 2020, wannesm/dtaidistance v2.0.0. doi:10.5281/zenodo.3981067

Merkin V. G., Lyon J. G., Lario D., Arge C. N., Henney C. J., 2016, J. Geophys. Res., 121, 2866

Nichols J. D., Cowley S. W. H., McComas D. J., 2006, Ann. Geophys., 24, 393

Nichols J. D., Clarke J. T., Gérard J. C., Grodent D., Hansen K. C., 2009, J. Geophys., Space Phys., 114, A06210

Nichols J. D. et al., 2017, Geophys. Res. Lett., 44, 7643

Odstrcil D., 2003, Adv. Space Res., 32, 497

Owens M. J., 2018, Space Weather, 16, 1847

Owens M., 2019, in Foster B., ed., Oxford Research Encyclopedia of Physics. Oxford Univ. Press, Oxford

Owens M. J., Arge C. N., Spence H. E., Pembroke A., 2005, J. Geophys. Res., 110, 1

Owens M. J. et al., 2008, Space Weather, 6, S08001

Owens M. J. et al., 2020, Sol. Phys., 295, 43

Pomoell J., Poedts S., 2018, J. Space Weather Space Clim., 8, A35

Prchlik J., Stevens M. L., 2018, AGU Fall Meeting Abstract, #SH43F-3737

Provan G., Tao C., Cowley S. W. H., Dougherty M. K., Coates A. J., 2015, J. Geophys., Space Phys., 120, 9524

Riley P., Linker J. A., Mikic Z., 2001, J. Geophys. Res., 106, 15889

Sakoe H., Chiba S., 1978, IEEE Trans. Acoust. Speech Signal Process., 26, 43

Tao C., Kataoka R., Fukunishi H., Takahashi Y., Yokoyama T., 2005, J. Geophys. Res., Space Phys., 110, A11208

Thomas S. R., Fazakerley A., Wicks R. T., Green L., 2018, Space Weather, 16, 814

Toth G. et al., 2005, J. Geophys. Res., 110, A12226
Turner H., Owens M., Lang M., Gonzi S., 2021, Space Weather, 19, e2021SW002802
Vennerstrom S., Olsen N., Purucker M., Acuña M. H., Cain J. C., 2003, Geophys. Res. Lett., 30, 1369
Zarka P., Lamy L., Cecconi B., Prangé R., Rucker H. O., 2007, Nature, 450, 265
Zieger B., Hansen K. C., 2008, J. Geophys. Res., 113, 8107

This paper has been typeset from a TEX/LATEX file prepared by the author.